Article

A highly magnetized and rapidly rotating white dwarf as small as the Moon

https://doi.org/10.1038/s41586-021-03615-y

Received: 27 October 2020

Accepted: 5 May 2021

Published online: 30 June 2021

Check for updates

Ilaria Caiazzo[1]✉, Kevin B. Burdge[1], James Fuller[1], Jeremy Heyl[2], S. R. Kulkarni[1], Thomas A. Prince[1], Harvey B. Richer[2], Josiah Schwab[3], Igor Andreoni[1], Eric C. Bellm[4], Andrew Drake[1], Dmitry A. Duev[1], Matthew J. Graham[1], George Helou[5], Ashish A. Mahabal[1,6], Frank J. Masci[5], Roger Smith[7] & Maayane T. Soumagnac[8,9]

White dwarfs represent the last stage of evolution of stars with mass less than about eight times that of the Sun and, like other stars, are often found in binaries[1,2]. If the orbital period of the binary is short enough, energy losses from gravitational-wave radiation can shrink the orbit until the two white dwarfs come into contact and merge[3]. Depending on the component masses, the merger can lead to a supernova of type Ia or result in a massive white dwarf[4]. In the latter case, the white dwarf remnant is expected to be highly magnetized[5,6] because of the strong magnetic dynamo that should arise during the merger, and be rapidly spinning from the conservation of the orbital angular momentum[7]. Here we report observations of a white dwarf, ZTF J190132.9+145808.7, that exhibits these properties, but to an extreme: a rotation period of 6.94 minutes, a magnetic field ranging between 600 megagauss and 900 megagauss over its surface, and a stellar radius of 2140^{+160}_{-230} kilometres, only slightly larger than the radius of the Moon. Such a small radius implies that the star's mass is close to the maximum white dwarf mass, or Chandrasekhar mass. ZTF J190132.9+145808.7 is likely to be cooling through the Urca processes (neutrino emission from electron capture on sodium) because of the high densities reached in its core.

Using the Zwicky Transient Facility[8] (ZTF), we searched for short-period objects that lie below the main white dwarf cooling sequence in the Gaia[9] colour–magnitude diagram (see Fig. 1). ZTF J190132.9+145808.7 (hereafter ZTF J1901+1458) showed promising small photometric variations. Follow-up with CHIMERA[10], a high-speed imaging photometer on the 200-inch Hale telescope, confirmed a period of 6.94 min (see Fig. 2). The period of ZTF J1901+1458 is unusually short for a white dwarf, as white dwarf rotational periods typically are upwards of hours[11]. The period and ephemeris are listed in Table 1.

We undertook phase-resolved spectroscopy using the Low Resolution Imaging Spectrometer (LRIS)[12] on the 10-m W. M. Keck I Telescope. As can be seen from Fig. 3, the phase-averaged spectrum exhibits broad and shallow features that we identify as hydrogen absorption lines in a high magnetic field. The presence of a strong magnetic field results in splitting and proportional shifting of the zero-field energy levels, leading to line broadening. To identify the field strength, we considered all the allowed bound–bound hydrogen transitions (tabulated in ref. [13]) and, as shown in Fig. 3, we find a satisfactory explanation for the spectrum. The identified spectral lines are listed in Extended Data Table 2.

We find that most of the spectral features are well characterized by a magnetic field strength of 800 million gauss (MG; red horizontal line in Fig. 3), comparable to the field detected on the most magnetic white dwarfs known[14]. As the absorption features indicate an average field strength over the surface, the field at the magnetic pole is bound to be higher. From the phase-resolved spectra (Extended Data Figs. 4 and 5), we see that some of the features become narrower or broader depending on the phase, and the feature at ~4,600 Å shifts in wavelength, which accounts for the dip at ~4,500 Å in the co-added spectrum. This means that in some regions of the surface, the magnetic field is as low as 600 MG. The explanation for the photometric variation, confirmed by the variations of absorption features with phase, is thus the combination of magnetic dichroism and rotation: the high magnetic field causes variations in the continuum opacities and in the surface temperature, and therefore, as the star rotates, we detect changes in flux as a function of the field strength across the stellar surface. Depending on the magnetic field configuration, this dichroism can account for up to 10% photometric variation[15], so it can easily account for the 3% amplitude observed in ZTF J1901+1458. The period of ZTF J1901+1458 could also be consistent with non-radial pulsations; however, its temperature and surface gravity place it far away from theoretical predictions for known instabilities (see Fig. 1), and its magnetic field may be strong enough to suppress gravity-mode (g-mode) pulsations (see Methods for further discussion).

[1]Division of Physics, Mathematics and Astronomy, California Institute of Technology, Pasadena, CA, USA. [2]Department of Physics and Astronomy, University of British Columbia, Vancouver, British Columbia, Canada. [3]Department of Astronomy and Astrophysics, University of California, Santa Cruz, CA, USA. [4]Department of Astronomy, University of Washington, Seattle, WA, USA. [5]IPAC, California Institute of Technology, Pasadena, CA, USA. [6]Center for Data Driven Discovery, California Institute of Technology, Pasadena, CA, USA. [7]Caltech Optical Observatories, California Institute of Technology, Pasadena, CA, USA. [8]Lawrence Berkeley National Laboratory, Berkeley, CA, USA. [9]Department of Particle Physics and Astrophysics, Weizmann Institute of Science, Rehovot, Israel. ✉e-mail: ilariac@caltech.edu

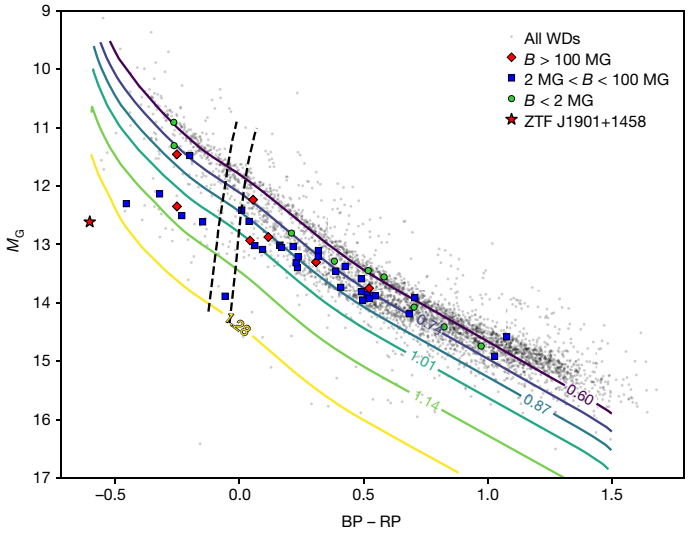

Fig. 1 | Gaia colour–magnitude diagram. Gaia colour–magnitude diagram for the white dwarfs that are within 100 pc from Earth and within the SDSS footprint[28], where the *x*-axis depicts the difference between the Gaia BP and RP bands, and the *y*-axis the absolute magnitude in the Gaia G filter. Solid lines show theoretical cooling tracks for white dwarfs (WDs) with masses between 0.6 $M_\odot$ (top) and 1.28 $M_\odot$ (bottom), equally spaced in mass; the atmosphere is assumed to be hydrogen-dominated[29] and the interior composition to be carbon–oxygen[30] for $M < 1.1\,M_\odot$ and oxygen–neon[19] for $M > 1.1\,M_\odot$. Coloured markers indicate white dwarfs for which a magnetic field was measured[14]. ZTF J1901+1458 is shown as a red star, and its location in the colour–magnitude diagram reveals its high mass. Vertical dashed lines indicate the location of the ZZ Ceti instability strip[31] (the pre-white dwarf, or DOV, instability strip lies above the plot[32,33]). Reddening corrections were applied only to ZTF J1901+1458; as the objects in the sample are close, reddening is expected to be small. 1σ error bars are smaller than the size of the coloured markers and are omitted from the black background dots for clarity.

Table 1 | ZTF J1901+1458 parameters

Parameter	Value
Gaia ID	4506869128279648512
Parallax (mas)	24.13 ± 0.06
μ_{RA} (mas yr^{-1})	95.50 ± 0.09
μ_{DEC} (mas yr^{-1})	72.45 ± 0.09
T_{eff} (K)	$46{,}000^{+19{,}000}_{-8{,}000}$
T_0 (*g*) (BMJD$_{TDB}$)	59079.217290 ± 0.000012
T_0 (*r*) (BMJD$_{TDB}$)	59079.21670 ± 0.00006
R_* (km)	$2{,}140^{+160}_{-230}$
M ($M_\odot$)	1.327 ± 1.365
$E(B-V)$	$0.044^{+0.017}_{-0.015}$
P (s)	416.2427 ± 0.0002
$\dot{P}$ (s s^{-1})	<10^{-11}

μ_{RA} and μ_{DEC}, proper motion; P, period. The ephemeris T_0 (barycentric modified Julian date in barycentric dynamical time, BMJD$_{TBD}$) corresponds to a minimum in the lightcurve. It is given separately for the ZTF *g*-band and *r*-band because the latter lags behind the former by 51 s. Here, T_0 corresponds to the minimum of each lightcurve.

To determine the temperature and radius of the white dwarf, we obtained photometric measurements in the near-ultraviolet using the UVOT (Ultraviolet/Optical Telescope) instrument[16] on the Neil Gehrels Swift Observatory[17], while the Pan-STARRS Survey[18] (PS1) and the Gaia mission provided optical photometry and parallax, respectively. We estimated the temperature, reddening and radius from the photometry, by comparing the observations with non-magnetic white dwarf atmosphere models. Because the white dwarf is very hot, the photometric constraints on the temperature are weak; however, the precise distance measurement from Gaia allows us to obtain a good estimate for the radius. We found the effective temperature, stellar radius and interstellar reddening to be $T_{eff} = 46{,}000^{+19{,}000}_{-8{,}000}$ K, $R_* = 2{,}140^{+160}_{-230}$ km and $E(B-V) = 0.044^{+0.017}_{-0.015}$, respectively (see Methods). The radius is smaller than those measured for other white dwarfs and only slightly larger than that of the Moon. As explained below, the small radius also means that ZTF J1901+1458 may be the most massive white dwarf yet discovered.

The mass can be inferred from the mass–radius relation which, as can be seen in Fig. 4, is composition-dependent. White dwarf descendants of single stars with mass above 1.1 solar masses ($M_\odot$) are expected to be mostly oxygen and neon, with traces of carbon, sodium and magnesium[19,20]. Even if born from a merger, compressional heating due to rapid accretion is expected to ignite off-centre carbon burning[21], resulting in an O/Ne white dwarf[7]. We conclude that, depending on the composition, ZTF J1901+1458 has a mass between 1.327 $M_\odot$ and 1.365 $M_\odot$.

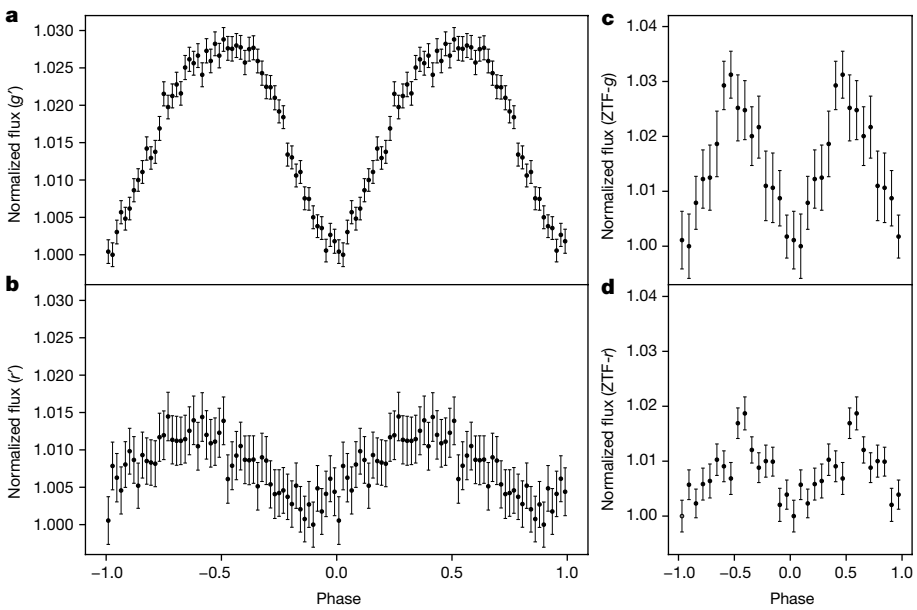

Fig. 2 | ZTF J1901+1458 lightcurve. a, **b**, The binned CHIMERA lightcurve phase-folded at a period of 6.94 min in the *g*′-band (**a**) and in the *r*′-band (**b**). The flux has been normalized to the minimum of the lightcurve in each band. The amplitude of the photometric variation is higher in the *g*′-band (about 3% peak-to-peak) than in the *r*′-band (~1.5%). Additionally, the two filters show a difference in phase: the red lags the green by about 51 s. **c**, **d**, The similarly normalized ZTF discovery lightcurve in the ZTF *g*-band (**c**) and *r*-band (**d**). The error bars indicate 1σ errors.

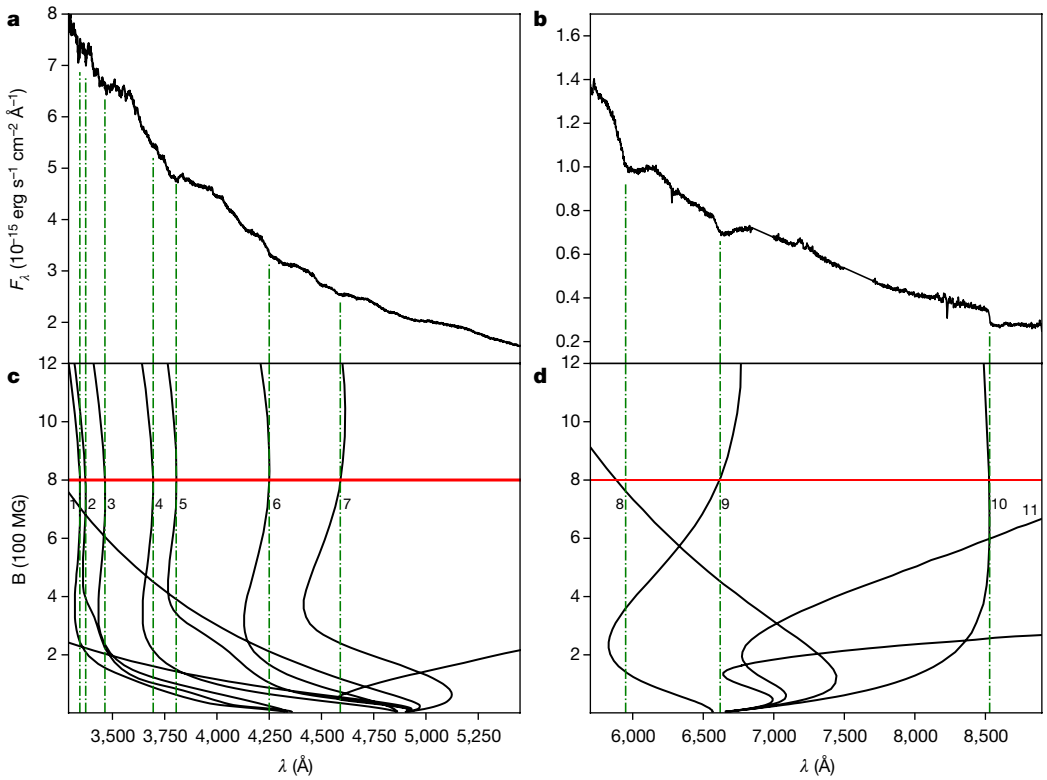

Fig. 3 | ZTF J1901+1458 optical spectrum. a, **b**, The LRIS phase-averaged spectrum of ZTF J1901+1458 is shown in black in the upper panels for the blue (**a**) and red (**b**) sections. **c**, **d**, The spectrum is compared to predicted line positions of Hα, Hβ and Hγ as a function of magnetic field[13], showing that the white dwarf is characterized by a field strength of about 800 MG (red horizontal solid line). The identified absorption features are highlighted by the green dot-dashed lines and numbered, and the respective transitions are listed in Extended Data Table 2.

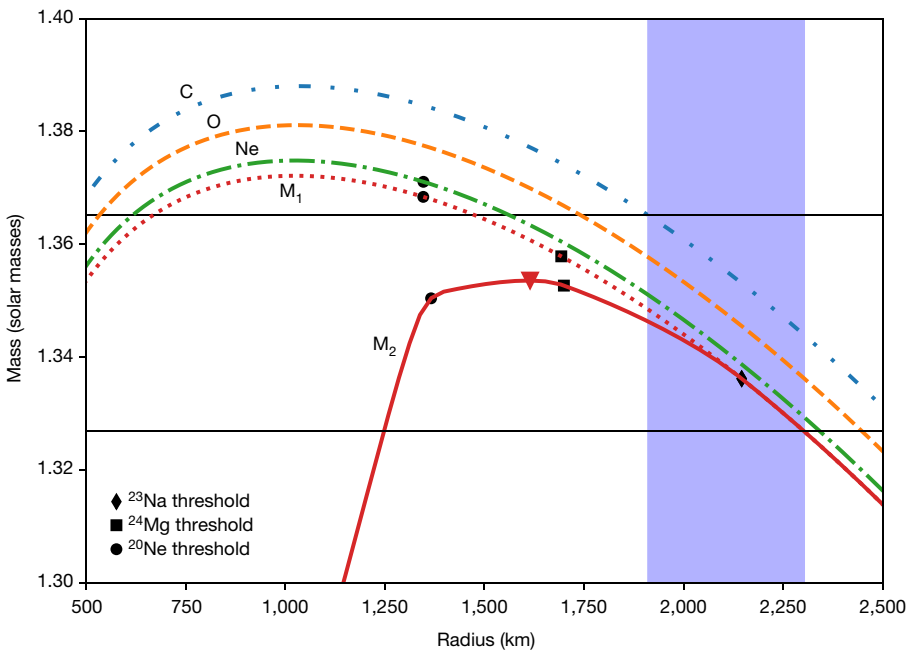

Fig. 4 | Mass–radius relation. The white dwarf mass–radius relation at the temperature of ZTF J1901+1458 (~46,000 K) is shown for different homogeneous compositions, neglecting the effect of electron captures: carbon C; oxygen O; neon Ne; and the mixture that is thought to result from carbon burning (M_1), specifically 58% oxygen, 30% neon, 2% carbon, 5% sodium and 5% magnesium[19]. The lowermost red solid curve (M_2) traces the result from the carbon-burning ash mixture, including the effect of electron captures (see text). The black marks along each track indicate the radius at which the central density reaches the threshold for inverse beta decay of Ne (circles), Mg (squares) and Na (diamonds). The vertical blue-shaded area indicates the observed radius of ZTF J1901+1458 within 1σ errors. The red triangle indicates the maximum mass of 1.354 $M_\odot$ at a radius of 1,600 km along the track of the mixed composition. The horizontal black solid lines highlight the mass of 1.365 $M_\odot$ determined using a radius of 1,910 km for the upper line (pure C), and 1.327 $M_\odot$ for a radius of 2,300 km for the lower line (carbon-burning ash mixture).

Two other extremely massive white dwarfs for which a radius has been measured are RE J0317−853[22] and WD1832+089[23], both with a radius of about 2,500 km. Curiously, they are both variable with short periods (6 min and 12 min, respectively). Whereas WD1832+089 does not show evidence for magnetism, RE J0317−853 appears to have a field that varies between 185 MG and 425 MG over its surface[15]. Thus both ZTF J1901+1458 and RE J0317−853, with their rapid rotation, high mass and magnetism, are likely to be remnants of a white dwarf merger.

At the densities reached in the centre of ZTF J1901+1458, the nuclei of some elements may undergo electron capture (also called inverse beta decay), removing electrons that contribute to the degeneracy pressure that keeps the star from collapsing. This lowers the maximum mass that can be sustained against gravity and reduces the equilibrium radius for a fixed mass (see Fig. 4, solid red curve). If ZTF J1901+1458 has an oxygen–neon internal composition (as is expected from its mass[7,19]), its central density is right at the threshold for electron capture on ^{23}Na, and its mass is within 2% of the highest possible mass for a white dwarf.

Neutrinos produced by inverse beta decay escape and carry away energy, contributing to the cooling of the white dwarf. Based on the luminosity of the white dwarf[19], we estimate the temperature in the core to be about $2–3 \times 10^7$ K. At such a high central temperature and density, the neutrino cooling of ZTF J1901+1458 will be dominated by the Urca process[24,25] acting on ^{23}Na. This unusual neutrino cooling makes an age determination difficult. A recent work[26] studied the evolution of Urca-cooling white dwarfs; from the same models, we estimate the cooling age of ZTF J1901+1458 to be between 10 and 100 Myr.

The mass–radius relation in Fig. 4 was calculated assuming that the core composition is homogeneous—a good assumption as ZTF J1901+1458 is less than 100 Myr old. However, over a few hundred million years, the heaviest elements, including Na, will gradually sink to the centre[27]. If the star lies at the small end of the radius constraints and if at least 60% of the ^{23}Na manages to sink and undergo beta decay before the core crystallizes and sedimentation stops, electron-capture on ^{24}Mg would ensue. The star would shrink and the internal pressure would no longer be able to support the star, as the maximum allowed mass for the new composition would be lower than the mass of the white dwarf (see Methods for a more detailed discussion). The star would therefore collapse and heat up, leading to the onset of electron capture onto Ne and to the ignition of oxygen nuclear burning. The white dwarf would then undergo a disruptive thermonuclear supernova or implode to form a neutron star[25].

The probability of collapse is highly uncertain, as it depends on the timescales of sedimentation and crystallization, both unconstrained at these high masses. However, the possibility of this new formation channel for neutron stars is intriguing. If, upon collapse, no angular momentum is lost and magnetic flux is conserved, the newly born neutron star, with a magnetic field strength of $\sim 2 \times 10^{13}$ G and a spin period of ~15 ms, would resemble a young pulsar. Owing to the gradual collapse, the neutron star would probably not receive a strong natal velocity kick. We would therefore expect such a neutron star population to be more concentrated to the galactic plane. Furthermore, the proximity of ZTF J1901+1458 (41 parsecs) means it is not a rare type of object, and thus this formation channel would contribute appreciably to the total neutron star population. ZTF is currently discovering large numbers of similarly massive and rapidly variable white dwarfs. This enlarged sample will help us better understand the origin and fate of such objects.

Online content

Any methods, additional references, Nature Research reporting summaries, source data, extended data, supplementary information, acknowledgements, peer review information; details of author contributions and competing interests; and statements of data and code availability are available at https://doi.org/10.1038/s41586-021-03615-y.

1. Brown, W. R. et al. The ELM Survey. VIII. Ninety-eight double white dwarf binaries. *Astrophys. J.* **889**, 49 (2020).
2. Burdge, K. B. et al. A systematic search of Zwicky Transient Facility data for ultracompact binary LISA-detectable gravitational-wave sources. *Astrophys. J.* **905**, 32 (2020).
3. Shen, K. J. Every interacting double white dwarf binary may merge. *Astrophys. J. Lett.* **805**, L6 (2015).
4. Dan, M., Rosswog, S., Brüggen, M. & Podsiadlowski, P. The structure and fate of white dwarf merger remnants. *Mon. Not. R. Astron. Soc.* **438**, 14–34 (2014).
5. Tout, C. A. et al. Binary star origin of high field magnetic white dwarfs. *Mon. Not. R. Astron. Soc.* **387**, 897–901 (2008).
6. Garca-Berro, E. et al. Double degenerate mergers as progenitors of high-field magnetic white dwarfs. *Astrophys. J.* **749**, 25 (2012).
7. Schwab, J. Evolutionary models for the remnant of the merger of two carbon-oxygen core white dwarfs. *Astrophys. J.* **906**, 53 (2021).
8. Bellm, E. C. et al. The Zwicky Transient Facility: system overview, performance, and first results. *Publ. Astron. Soc. Pacif.* **131**, 018002 (2019).
9. Gaia Collaboration et al. The Gaia mission. *Astron. Astrophys.* **595**, A1 (2016).
10. Harding, L. K. et al. CHIMERA: a wide-field, multi-colour, high-speed photometer at the prime focus of the Hale telescope. *Mon. Not. R. Astron. Soc.* **457**, 3036–3049 (2016).
11. Hermes, J. J. et al. White dwarf rotation as a function of mass and a dichotomy of mode line widths: Kepler observations of 27 pulsating DA white dwarfs through K2 Campaign 8. *Astrophys. J. Suppl.* **232**, 23 (2017).
12. Oke, J. B. et al. The Keck Low-Resolution Imaging Spectrometer. *Publ. Astron. Soc. Pacif.* **107**, 375 (1995).
13. Ruder, H., Wunner, G., Herold, H. & Geyer, F. *Atoms in Strong Magnetic Fields. Quantum Mechanical Treatment and Applications in Astrophysics and Quantum Chaos* (Springer, 1994).
14. Ferrario, L., de Martino, D. & Gänsicke, B. T. Magnetic white dwarfs. *Space Sci. Rev.* **191**, 111–169 (2015).
15. Ferrario, L. et al. EUVE J0317–855: a rapidly rotating, high-field magnetic white dwarf. *Mon. Not. R. Astron. Soc.* **292**, 205–217 (1997).
16. Roming, P. W. A. et al. The Swift Ultra-Violet/Optical Telescope. *Space Sci. Rev.* **120**, 95–142 (2005).
17. Gehrels, N. et al. The Swift Gamma-Ray Burst Mission. *Astrophys. J.* **611**, 1005–1020 (2004).
18. Chambers, K. C. et al. The Pan-STARRS1 Surveys. Preprint at https://arxiv.org/abs/1612.05560 (2016).
19. Camisassa, M. E. et al. The evolution of ultra-massive white dwarfs. *Astron. Astrophys.* **625**, A87 (2019).
20. Siess, L. Evolution of massive AGB stars. II. Model properties at non-solar metallicity and the fate of super-AGB stars. *Astron. Astrophys.* **476**, 893–909 (2007).
21. Shen, K. J., Bildsten, L., Kasen, D. & Quataert, E. The long-term evolution of double white dwarf mergers. *Astrophys. J.* **748**, 35 (2012).
22. Külebi, B., Jordan, S., Nelan, E., Bastian, U. & Altmann, M. Constraints on the origin of the massive, hot, and rapidly rotating magnetic white dwarf RE J 0317–853 from an HST parallax measurement. *Astron. Astrophys.* **524**, A36 (2010).
23. Pshirkov, M. S. et al. Discovery of a hot ultramassive rapidly rotating DBA white dwarf. *Mon. Not. R. Astron. Soc.* **499**, L21–L25 (2020).
24. Tsuruta, S. & Cameron, A. G. W. URCA shells in dense stellar interiors. *Astrophys. Space Sci.* **7**, 374–406 (1970).
25. Schwab, J., Bildsten, L. & Quataert, E. The importance of Urca-process cooling in accreting ONe white dwarfs. *Mon. Not. R. Astron. Soc.* **472**, 3390–3406 (2017).
26. Schwab, J. Cooling models for the most massive white dwarfs. *Astrophys. J.* (in the press).
27. Deloye, C. J. & Bildsten, L. Gravitational settling of ^{22}Ne in liquid white dwarf interiors: cooling and seismological effects. *Astrophys. J.* **580**, 1077–1090 (2002).
28. Kilic, M. et al. The 100 pc white dwarf sample in the SDSS footprint. *Astrophys. J.* **898**, 84 (2020).
29. Holberg, J. B. & Bergeron, P. Calibration of synthetic photometry using DA white dwarfs. *Astron. J.* **132**, 1221–1233 (2006).
30. Fontaine, G., Brassard, P. & Bergeron, P. The potential of white dwarf cosmochronology. *Publ. Astron. Soc. Jpn* **113**, 409–435 (2001).
31. Van Grootel, V. et al. The instability strip of ZZ Ceti white dwarfs. I. Introduction of time-dependent convection. *Astron. Astrophys.* **539**, A87 (2012).
32. Maeda, K. & Shibahashi, H. Pulsations of pre-white dwarfs with hydrogen-dominated atmospheres. *Publ. Astron. Soc. Pacif.* **66**, 76 (2014).
33. Quirion, P. O., Fontaine, G. & Brassard, P. Wind competing against settling: a coherent model of the GW Virginis instability domain. *Astrophys. J.* **755**, 128 (2012).

Methods

Period detection

Our search for periodicity in massive white dwarfs was part of a broader search for periodic variability on and around the white dwarf cooling track with ZTF, which has already yielded several results, including finding numerous double white dwarf binaries[2,34,35]. The targets were selected using the Pan-STARRS (PS1) source catalogue[18], cross-matched with a white dwarf catalogue[36], after imposing a photometric colour selection of $(g-r)<0.2$ and $(r-i)<0.2$. As the sensitivity of period finding depends strongly on the number of samples in the lightcurve, we limited the search to those targets for which 50 or more photometric 5σ detections are available in the ZTF archival data. To maximize the number of epochs for each lightcurve, we combined data from multiple filters by computing the median magnitude in each filter and shifting the *g*- and *i*-bands so that their median magnitude matched the *r*-band data. We used a graphics processing unit (GPU) implementation of the conditional entropy period-finding algorithm[37]. We cross-matched our candidates with the Gaia DR2 catalogue[38] and visually inspected the lightcurves of those objects that lie below the main white dwarf cooling track in the Gaia colour–magnitude diagram. ZTF J1901+1458 stood out because of the high-significance detection of its short period, and its blue and faint location in the colour–magnitude diagram (see Fig. 1).

Magnetic field

At low magnetic field strengths, the effect of magnetic field on hydrogen transitions can be calculated as a perturbation to the zero-field electron wavefunction. The perturbation lifts the degeneracy in the *m* quantum number, and each transition is split into three Zeeman components, corresponding to a change in *m* of +1, 0 and −1. In the strong regime (above ~100 MG), the magnetic and Coulomb terms are comparable, and the wavefunction no longer has spherical symmetry. The perturbation method is not viable in this case, and the energies and oscillator strengths of hydrogen transitions in this regime were calculated using variational methods[39–42]. An important characteristic of high-field transitions is that some transitions become 'stationary'—that is, they go through a minimum or a maximum in energy—and, at those field strengths, appreciable changes in **B** yield only small changes in wavelength. The magnetic broadening at these transitions is considerably reduced, and therefore the absorption features are still detectable even after averaging the field over the surface of the white dwarf. We considered all the bound–bound transitions tabulated in ref. [13] that follow selection rules, and we found that the features in the spectrum of ZTF J1901+1458 correspond to stationary lines in a field of ~800 MG. The wavelengths of the transitions in this regime as a function of magnetic field strength are shown in the lower panels of Fig. 3. The identified features are numbered and the corresponding transitions are listed in Extended Data Table 2, where the states are labelled by their asymptotic quantum numbers *nlm* for the zero-field states and by the numbers $NM\mu$ for $B\rightarrow\alpha$, where μ defines the *z* parity of the states ($\pi=(-1)^{\mu}$). A few lines show variations with phase (see Extended Data Figs. 4 and 5), which can be attributed to the variation of the magnetic field strength across the surface. In particular, some of the features become narrower or broader at different times, indicating that the field is more or less uniform over the surface at different rotation phases. Additionally, the feature at ~4,600 Å (line 7) shifts in wavelength, going as low as ~4,500 Å, which indicates that the magnetic field is as low as 600 MG on some regions on the surface of the white dwarf. This is also confirmed by the contamination of line 10 by line 11.

Photometric fitting

To determine the radius and effective temperature of ZTF J1901+1458, we made use of the available Pan-STARRS[18] photometry and the Gaia[9,38] parallax. In addition, we obtained Swift[17] UVOT[16] photometry (TOO proposal number 14380, target ID 13650). The photometric data used in the fitting are listed in Extended Data Table 1. As the errors in the Pan-STARRS photometry are lower than the photometric variation, we used an error of 0.02 magnitudes instead to take into account the error induced by variability. To estimate the temperature and reddening, we fitted the photometric data with the white dwarf 1D model DA (hydrogen-dominated) atmospheres of ref. [43]. The value of the radius is then estimated thanks to the parallax measurement from Gaia.

To account for extinction, we applied reddening corrections to the synthetic spectra (and polynomials) using the extinction curves of ref. [44] (available at https://www.stsci.edu/). From the corrected models, we computed synthetic photometry using the pyphot package (https://mfouesneau.github.io/docs/pyphot/).

For the fit, we used a Levenberg-Marquardt algorithm, and the free parameters were the effective temperature $T_{\rm eff}$ and radius R_* of the white dwarf as well as the interstellar reddening $E(B-V)$. For the reddening, we imposed a prior based on the distribution of interstellar extinction measured by Gaia for the stars in the same area of the sky as ZTF J1901+1458. In particular, we selected the stars that are within 5 degrees of the location of white dwarf and within 50 pc from Earth (see Extended Data Fig. 2). The best fit is shown in Extended Data Fig. 1, while the left panel of Extended Data Fig. 3 illustrates the corner plots. In the fit, we assumed the nominal value of the Gaia parallax for the distance. As a change in distance would have the effect of changing the normalization in the spectrum, the error in the distance only influences the error in the stellar radius, and therefore we included the error in the distance in the error in the radius. The errors quoted are the statistical errors derived from the Monte Carlo simulation shown in Extended Data Fig. 3. They do not include possible modelling errors due to the effect of the magnetic field; however, as the photometric variation is small, we do not expect the magnetic field to introduce a significant error on the synthetic values.

To verify whether our estimates are robust against the uncertainties in the spectral models, we used a different set of models for hydrogen-dominated atmospheres, the ones developed by ref. [45], and performed the same analysis introduced above. The results are shown in the right panel of Extended Data Fig. 3: the estimates of temperature, radius and reddening all agree within the 1σ errors. Magnetic models that tackle the effects of magnetic field on the continuum opacities are currently unavailable, and therefore we cannot estimate the errors due to neglecting the field.

Theoretical mass–radius relation

To derive the mass of the white dwarf, we computed the mass–radius relation using an equation of state that includes Coulomb corrections to the pressure and energy of a degenerate Fermi gas[46,47], as done in ref. [48]. As ZTF J1901+1458 is so compact, general relativistic corrections are important and therefore, contrary to ref. [48], we did not integrate the Newtonian hydrostatic equilibrium equation, but rather the Tolman–Oppenheimer–Volkoff (TOV) equation[49,50]. The results are shown in Fig. 4 for several compositions. Our calculations were performed assuming the zero-temperature limit because the temperature of the white dwarf is insufficient to change its structure significantly. For the composition of the carbon-burning ash, we use the results from ref. [19]. For the density thresholds for the electron capture onto magnesium and neon[51], we use values of 4×10^9 g cm^{-3} and 9×10^9 g cm^{-3} respectively. For sodium[25], we use 1.7×10^9 g cm^{-3}. We estimate the temperature at a density of 1.7×10^9 g cm^{-3} to be about 3×10^7 K; therefore, the neutrino cooling of ZTF J1901+1458, unlike for all other known white dwarfs, is dominated by the Urca process on ^{23}Na (refs. [24,25]), which makes an age determination difficult. A recent work[26] simulated the evolution of Urca-cooling white dwarfs with the Modules for Experiments in Stellar Astrophysics code (MESA)[52–56], showing that the Urca processes are the main cooling mechanism in the core of stars like ZTF J1901+1458 when they are younger than about 30 Myr. From the same models, we can estimate the cooling age of the white dwarf to be between 10 and 100 Myr.

Sedimentation and collapse

The solid red curve in Fig. 4 was calculated assuming that the core composition of the white dwarf is homogeneous and that all the sodium currently at densities above the threshold for electron capture has already undergone inverse beta decay, and similarly for magnesium and neon. As the sedimentation proceeds, much of the remaining ^{23}Na will sink to densities above the threshold and undergo beta decay, reducing the number of electrons in the star and reducing its radius. This means that the solid red curve in Fig. 4 will be lowered, because the equilibrium radius for any given mass will be smaller, and therefore the red triangle (the maximum mass allowed) will sink. This process can only be stopped if the core crystallizes before enough sodium can reach the centre, as crystallization would de facto freeze the composition gradient. If the star lies at the small end of the radius constraint and if at least 60% of the ^{23}Na manages to sink and decay before the core crystallizes, electron capture on ^{24}Mg would ensue and the radius of the white dwarf would shrink to about 1,550 km. The central density at this point would be 6×10^9 g cm^{-3}, still below the threshold for electron capture on neon, but the mass of the white dwarf would be above the maximum mass (the red triangle in Fig. 4 would have sunk below the current white dwarf mass). The internal pressure would be then insufficient to support the star, and the star would begin to collapse, heat up and start electron capture onto neon and nuclear burning of oxygen.

The possibility of collapse is highly uncertain as it depends on the timescales for crystallization and for the sedimentation of sodium, both currently poorly constrained, especially for such an extremely massive white dwarf.

Origin of photometric variability

The photometric variability of ZTF J1901+1458 may arise from either rotation or pulsations, but we believe rotational modulation is more likely. A large fraction of the hot DQs (hot white dwarfs with carbon-dominated atmospheres) are magnetic and photometrically variable, often with periods of several minutes[57,58]. Although ZTF J1901+1458 is not a DQ white dwarf, its other properties such as high mass, high temperature, high magnetic field and rotational modulation are similar to the hot DQ white dwarfs, albeit more extreme. A useful case study is that of the white dwarf SDSS J142625.71+575218.3, which varies with a period of $P \approx 418$ s (ref. [59]) and has a magnetic field strength of $B \approx 1.2$ MG (ref. [60]). Non-radial g-mode pulsations were originally thought to be responsible for the photometric modulation of SDSS J1426. Follow-up observations revealed a tentative additional periodicity at 318 s (ref. [61]), but additional data ruled out the existence of this periodicity and set stringent limits on additional periodicities in SDSS 1426 and other variable DQ white dwarfs[57]. This led Williams[57] to conclude that rotational modulation is the most likely source of variability in SDSS 1426 and other hot DQ white dwarfs. At present, there are no known strongly magnetic pulsating WDs, although some magnetic WDs could be pulsating below detectable levels.

Furthermore, the inferred temperature and surface gravity of ZTF J1901+1458 characterize it as an unlikely pulsator for known instability mechanisms. The temperature of ZTF J1901+1458, ~50,000 K, is much higher than the predicted blue edge of the ZZ Ceti instability strip, located at a temperature of about 12,500–14,000 K (refs. [31,62]) and of the helium white dwarf (DBV) instability strip, at about 30,000 K (ref. [63]) (the detection of hydrogen also discourages the DBV interpretation). The DOV or GW Vir instability strip includes similar and higher temperatures than what we found for ZTF J1901+1458, but both instability mechanisms involved, the $\kappa - \gamma$ mechanism for carbon and oxygen and the ε-mechanism for hydrogen, are inefficient at such high surface gravities (see for example Figure 8 of ref. [33] and Figure 6 of ref. [32]). It is also possible that magnetic fields suppress g-mode pulsations by converting gravity waves to Alfvén waves[64–67], which is likely to be the cause of suppressed dipole modes in red giant stars[68]. Follow-up work showed that magnetic fields greater than $B \approx 0.1$ MG are sufficient to suppress g modes of typical periods in ZZ Ceti stars[69], so magnetic suppression is a possibility for ZTF J1901+1458.

For these reasons, we believe the variability of ZTF J1901+1458 is most likely to be caused by rotation rather than pulsations, although we cannot rule out either mechanism. Follow-up observations can place more stringent limits on the presence of other non-harmonic periodicities that would be expected in the pulsation hypothesis. Finally, even if pulsations were the source of variability in ZTF J1901+1458, this would further enhance the extraordinary nature of this star by making it the most massive pulsating white dwarf and the only magnetic pulsating white dwarf known.

Data availability

Upon request, I.C. will provide the reduced photometric lightcurves and spectroscopic data, and available ZTF data for the object. The spectroscopic data and photometric lightcurves are also available in the GitHub repository https://github.com/ilac/ZTF-J1901-1458. ZTF data are accessible in the ZTF database. The astrometric and photometric data are already in the public domain, and they are readily accessible in the Gaia and Pan-STARSS catalogues and in the Swift database.

Code availability

We used the pyphot package (https://mfouesneau.github.io/docs/pyphot/) and the corner.py package[70]. The LRIS spectra were reduced using the Lpipe pipeline[71]. Upon request, I.C. will provide the code used to analyse the spectroscopic and photometric data.

34. Burdge, K. B. et al. General relativistic orbital decay in a seven-minute-orbital-period eclipsing binary system. *Nature* **571**, 528–531 (2019).
35. Burdge, K. B. et al. Orbital decay in a 20 minute orbital period detached binary with a hydrogen-poor low-mass white dwarf. *Astrophys. J. Lett.* **886**, L12 (2019).
36. Gentile Fusillo, N. P. & et al. A Gaia Data Release 2 catalogue of white dwarfs and a comparison with SDSS. *Mon. Not. R. Astron. Soc.* **482**, 4570–4591 (2019).
37. Graham, M. J., Drake, A. J., Djorgovski, S. G., Mahabal, A. A. & Donalek, C. Using conditional entropy to identify periodicity. *Mon. Not. R. Astron. Soc.* **434**, 2629–2635 (2013).
38. Gaia Collaboration et al. Gaia Data Release 2. Summary of the contents and survey properties. *Astron. Astrophys.* **616**, A1 (2018).
39. Rosner, W., Wunner, G., Herold, H. & Ruder, H. Hydrogen atoms in arbitrary magnetic fields. I. Energy levels and wavefunctions. *J. Phys. B* **17**, 29–52 (1984).
40. Forster, H. et al. Hydrogen atoms in arbitrary magnetic fields. II. Bound–bound transitions. *J. Phys. B* **17**, 1301–1319 (1984).
41. Henry, R. J. W. & Oconnell, R. F. Hydrogen spectrum in magnetic white dwarfs: H alpha, H beta and H gamma transitions. *Publ. Astron. Soc. Pacif.* **97**, 333–339 (1985).
42. Wunner, G., Roesner, W., Herold, H. & Ruder, H. Stationary hydrogen lines in white dwarf magnetic fields and the spectrum of the magnetic degenerate GRW + 70 8247. *Astron. Astrophys.* **149**, 102–108 (1985).
43. Tremblay, P. E., Bergeron, P. & Gianninas, A. An improved spectroscopic analysis of DA white dwarfs from the Sloan Digital Sky Survey Data Release 4. *Astrophys. J.* **730**, 128 (2011).
44. Cardelli, J. A., Clayton, G. C. & Mathis, J. S. The relationship between infrared, optical, and ultraviolet extinction. *Astrophys. J.* **345**, 245 (1989).
45. Bohlin, R. C., Hubeny, I. & Rauch, T. New grids of pure-hydrogen white dwarf NLTE model atmospheres and the HST/STIS flux calibration. *Astron. J.* **160**, 21 (2020).
46. Timmes, F. X. & Swesty, F. D. The accuracy, consistency, and speed of an electron–positron equation of state based on table interpolation of the Helmholtz free energy. *Astrophys. J.* **126** (Suppl.), 501–516 (2000).
47. Schwab, J. python-helmholtz: Python bindings for Frank Timmes' Helmholtz EoS. https://doi.org/10.5281/zenodo.4056084 (2020).
48. Hamada, T. & Salpeter, E. E. Models for zero-temperature stars. *Astrophys. J.* **134**, 683 (1961).
49. Tolman, R. C. Static solutions of Einstein's field equations for spheres of fluid. *Phys. Rev.* **55**, 364–373 (1939).
50. Oppenheimer, J. R. & Volkoff, G. M. On massive neutron cores. *Phys. Rev.* **55**, 374–381 (1939).
51. Miyaji, S., Nomoto, K., Yokoi, K. & Sugimoto, D. Supernova triggered by electron captures. *Publ. Astron. Soc. Jpn* **32**, 303–329 (1980).
52. Paxton, B. et al. Modules for Experiments in Stellar Astrophysics (MESA). *Astrophys. J. Suppl.* **192**, 3 (2011).
53. Paxton, B. et al. Modules for Experiments in Stellar Astrophysics (MESA): Planets, oscillations, rotation, and massive stars. *Astrophys. J. Suppl.* **208**, 4 (2013).
54. Paxton, B. et al. Modules for Experiments in Stellar Astrophysics (MESA): Binaries, pulsations, and explosions. *Astrophys. J. Suppl.* **220**, 15 (2015).
55. Paxton, B. et al. Modules for Experiments in Stellar Astrophysics (MESA): Convective boundaries, element diffusion, and massive star explosions. *Astrophys. J. Suppl.* **234**, 34 (2018).

56. Paxton, B. et al. Modules for Experiments in Stellar Astrophysics (MESA): Pulsating variable stars, rotation, convective boundaries, and energy conservation. *Astrophys. J. Suppl.* **243**, 10 (2019).
57. Williams, K. A., Montgomery, M. H., Winget, D. E., Falcon, R. E. & Bierwagen, M. Variability in hot carbon-dominated atmosphere (hot DQ) white dwarfs: rapid rotation? *Astrophys. J.* **817**, 27 (2016).
58. Ferrario, L., Wickramasinghe, D. & Kawka, A. Magnetic fields in isolated and interacting white dwarfs. *Adv. Space Res.* **66**, 1025–1056 (2020).
59. Montgomery, M. H. et al. SDSS J142625.71 + 575218.3: a prototype for a new class of variable white dwarf. *Astrophys. J. Lett.* **678**, L51 (2008).
60. Dufour, P., Fontaine, G., Liebert, J., Williams, K. & Lai, D. K. SDSS J142625.71 + 575218.3: the first pulsating white dwarf with a large detectable magnetic field. *Astrophys. J. Lett.* **683**, L167 (2008).
61. Green, E. M., Dufour, P., Fontaine, G. & Brassard, P. Follow-up studies of the pulsating magnetic white dwarf SDSS J142625.71 + 575218.3. *Astrophys. J.* **702**, 1593–1603 (2009).
62. Córsico, A. H., Althaus, L. G., Miller Bertolami, M. M. & Kepler, S. O. Pulsating white dwarfs: new insights. *Astron. Astrophys. Rev.* **27**, 7 (2019).
63. Beauchamp, A. et al. Spectroscopic studies of DB white dwarfs: the instability strip of the pulsating DB (V777 Herculis) stars. *Astrophys. J.* **516**, 887–891 (1999).
64. Fuller, J., Cantiello, M., Stello, D., Garcia, R. A. & Bildsten, L. Asteroseismology can reveal strong internal magnetic fields in red giant stars. *Science* **350**, 423–426 (2015).
65. Lecoanet, D., Vasil, G. M., Fuller, J., Cantiello, M. & Burns, K. J. Conversion of internal gravity waves into magnetic waves. *Mon. Not. R. Astron. Soc.* **466**, 2181–2193 (2017).
66. Loi, S. T. & Papaloizou, J. C. B. Effects of a strong magnetic field on internal gravity waves: trapping, phase mixing, reflection, and dynamical chaos. *Mon. Not. R. Astron. Soc.* **477**, 5338–5357 (2018).
67. Loi, S. T. Magneto-gravity wave packet dynamics in strongly magnetized cores of evolved stars. *Mon. Not. R. Astron. Soc.* **493**, 5726–5742 (2020).
68. Stello, D. et al. A prevalence of dynamo-generated magnetic fields in the cores of intermediate-mass stars. *Nature* **529**, 364–367 (2016).
69. Cantiello, M., Fuller, J. & Bildsten, L. Asteroseismic signatures of evolving internal stellar magnetic fields. *Astrophys. J.* **824**, 14 (2016).
70. Foreman-Mackey, D. corner.py: Scatterplot matrices in python. *J. Open Source Softw.* **1**, 24 (2016); https://doi.org/10.21105/joss.00024.
71. Perley, D. A. Fully automated reduction of longslit spectroscopy with the Low Resolution Imaging Spectrometer at the Keck Observatory. *Publ. Astron. Soc. Pacif.* **131**, 084503 (2019).

Acknowledgements The authors thank S.-C. Leung and S. Phinney for discussions, and N. Reindl and M. Kilic for comments. I.C. is a Sherman Fairchild Fellow at Caltech and thanks the Burke Institute at Caltech for supporting her research. J.F. acknowledges support through an Innovator Grant from the Rose Hills Foundation, and the Sloan Foundation through grant FG-2018-10515. K.B.B. thanks NASA and the Heising Simons Foundation for supporting his research. J.S. is supported by the A. F. Morrison Fellowship in Lick Observatory and by the US National Science Foundation (NSF) through grant ACI-1663688.

This work is based on observations obtained with the Samuel Oschin 48-inch telescope and the Palomar Observatory 60-inch telescope as part of the ZTF project. ZTF is supported by the NSF under grant no. AST-1440341 and a collaboration including Caltech, IPAC, the Weizmann Institute for Science, the Oskar Klein Center at Stockholm University, the University of Maryland, the University of Washington, Deutsches Elektronen-Synchrotron and Humboldt University, Los Alamos National Laboratories, the TANGO Consortium of Taiwan, the University of Wisconsin at Milwaukee, and Lawrence Berkeley National Laboratories. Operations are conducted by Caltech Optical Observatories, IPAC and the University of Washington. Some of the data presented herein were obtained at the W. M. Keck Observatory, which is operated as a scientific partnership among the California Institute of Technology, the University of California and NASA. This work has made use of data from the European Space Agency (ESA) mission Gaia (https://www.cosmos.esa.int/gaia), processed by the Gaia Data Processing and Analysis Consortium (DPAC; https://www.cosmos.esa.int/web/gaia/dpac/consortium). Funding for the DPAC has been provided by national institutions, in particular the institutions participating in the Gaia Multilateral Agreement. The Pan-STARRS1 Surveys (PS1) and the PS1 public science archive have been made possible through contributions by the Institute for Astronomy, the University of Hawaii, the Pan-STARRS Project Office, the Max Planck Society and its participating institutes, the Max Planck Institute for Astronomy, Heidelberg and the Max Planck Institute for Extraterrestrial Physics, Garching, The Johns Hopkins University, Durham University, the University of Edinburgh, the Queen's University Belfast, the Harvard-Smithsonian Center for Astrophysics, the Las Cumbres Observatory Global Telescope Network Incorporated, the National Central University of Taiwan, the Space Telescope Science Institute, NASA under grant no. NNX08AR22G issued through the Planetary Science Division of the NASA Science Mission Directorate, NSF grant no. AST-1238877, the University of Maryland, Eotvos Lorand University (ELTE), Los Alamos National Laboratory, and the Gordon and Betty Moore Foundation. This work was supported by the Natural Sciences and Engineering Research Council of Canada.

Author contributions I.C. reduced the ultraviolet data, conducted the spectral and photometric analysis, identified the magnetic field and is the primary author of the manuscript. K.B.B. performed the period search on ZTF data and reduced the optical data. I.C. and J.H. conducted the mass–radius analysis. I.C., K.B.B., J.F., J.H., S.R.K., T.A.P., H.B.R. and J.S. contributed to the physical interpretation of the object. J.S. constructed preliminary MESA models for the object. I.A., A.D., D.A.D., A.A.M., F.J.M., R.S. and M.T.S. contributed to the implementation of ZTF. G.H. is a co-PI of the ZTF Mid-Scale Innovations Program (MSIP). M.J.G. is the project scientist, E.C.B. is the survey scientist, T.A.P. is the co-PI and S.R.K. is the PI of ZTF.

Competing interests The authors declare no competing interests.

Additional information
Correspondence and requests for materials should be addressed to I.C.
Peer review information *Nature* thanks the anonymous reviewers for their contribution to the peer review of this work.
Reprints and permissions information is available at http://www.nature.com/reprints.

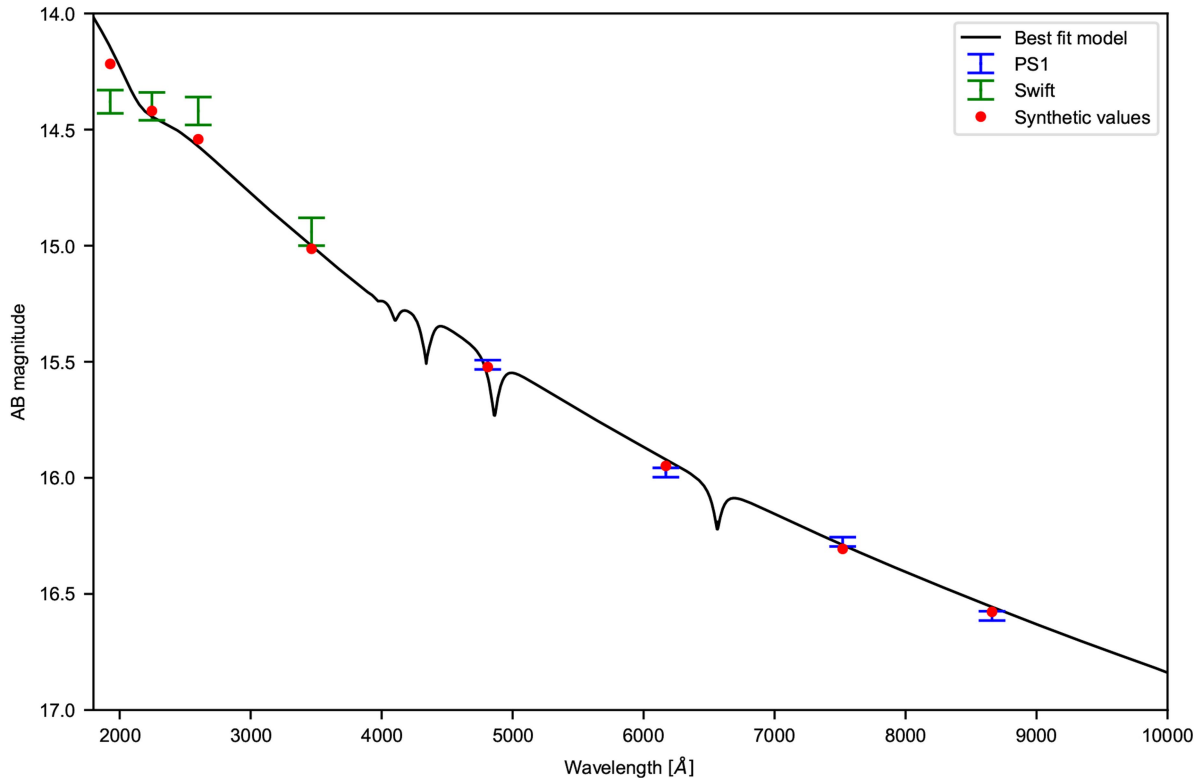

Extended Data Fig. 1 | Photometric fit. The blue solid line shows the best-fitting model spectrum, fitted to Pan-STARRS and Swift photometry to determine $T_{\rm eff}$, R_* and $E(B-V)$. The synthetic photometric values (obtained from the black line) are shown in red. The Swift values are shown in green with 1σ error bars and the Pan-STARRS values in blue with the error that we chose to account for the photometric variability (0.02 mag).

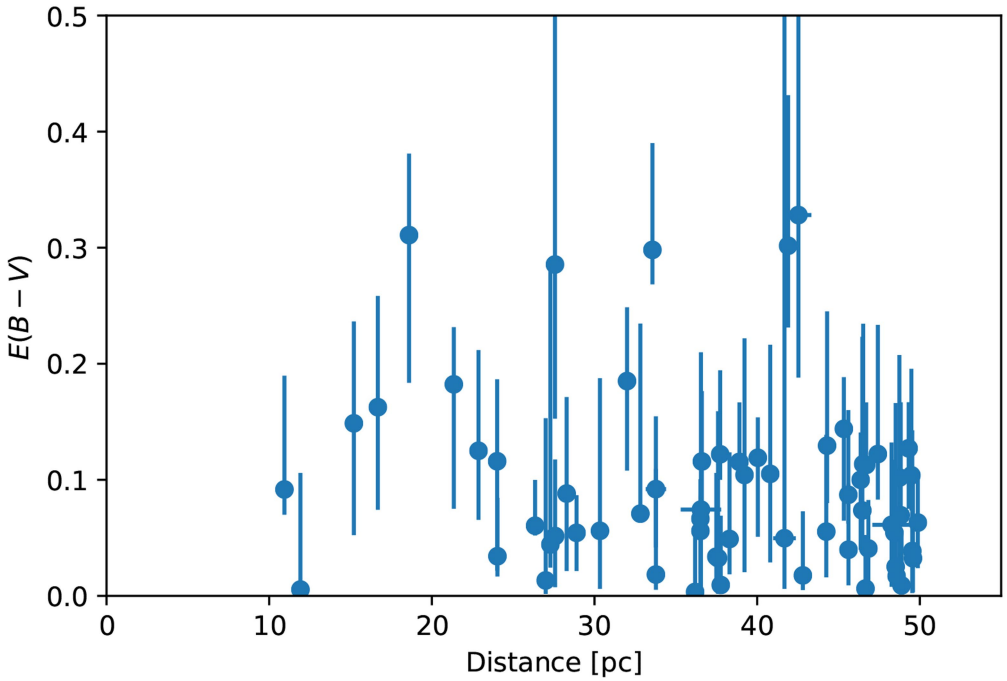

Extended Data Fig. 2 | Gaia $E(B-V)$ of the closest stars. The plot shows the extinction A_G as measured by Gaia of the stars within 5 degrees of ZTF 1901+1458 as a function of distance and converted to $E(B-V)$ assuming a reddening law with $R_V = 3.1$. We use the average reddening or the closest stars as a prior for the fitting. The error bars show 1σ errors.

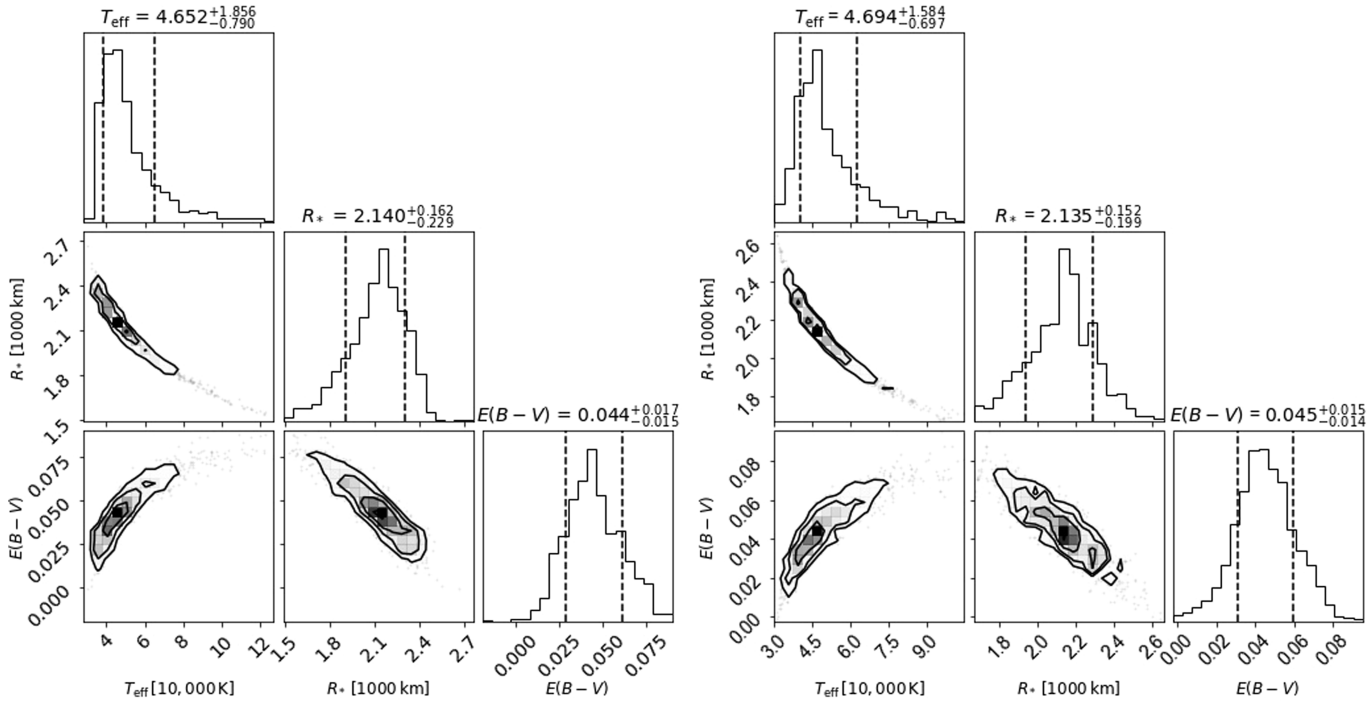

Extended Data Fig. 3 | Corner plots. Corner plots for the photometric fitting: results for the model atmospheres of Tremblay et al.[43] (left) and Bohlin et al.[45] (right).

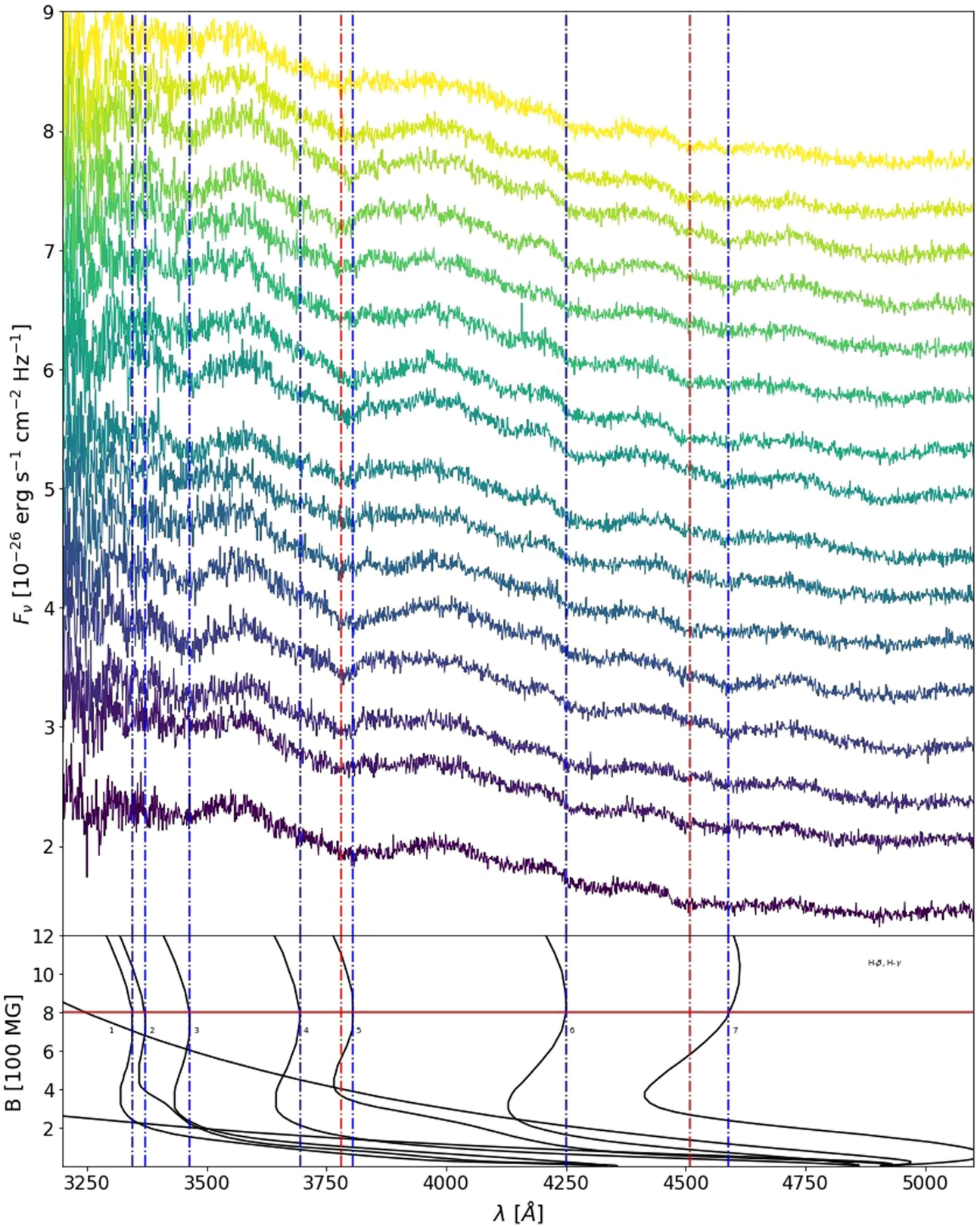

Extended Data Fig. 4 | Phase-resolved spectra, blue side. The LRIS phase-resolved spectra of ZTF J1901+1458 in the blue side. Some small variations can be observed in the spectral features with phase, especially in features at ~4,600 Å and at ~3,800 Å.

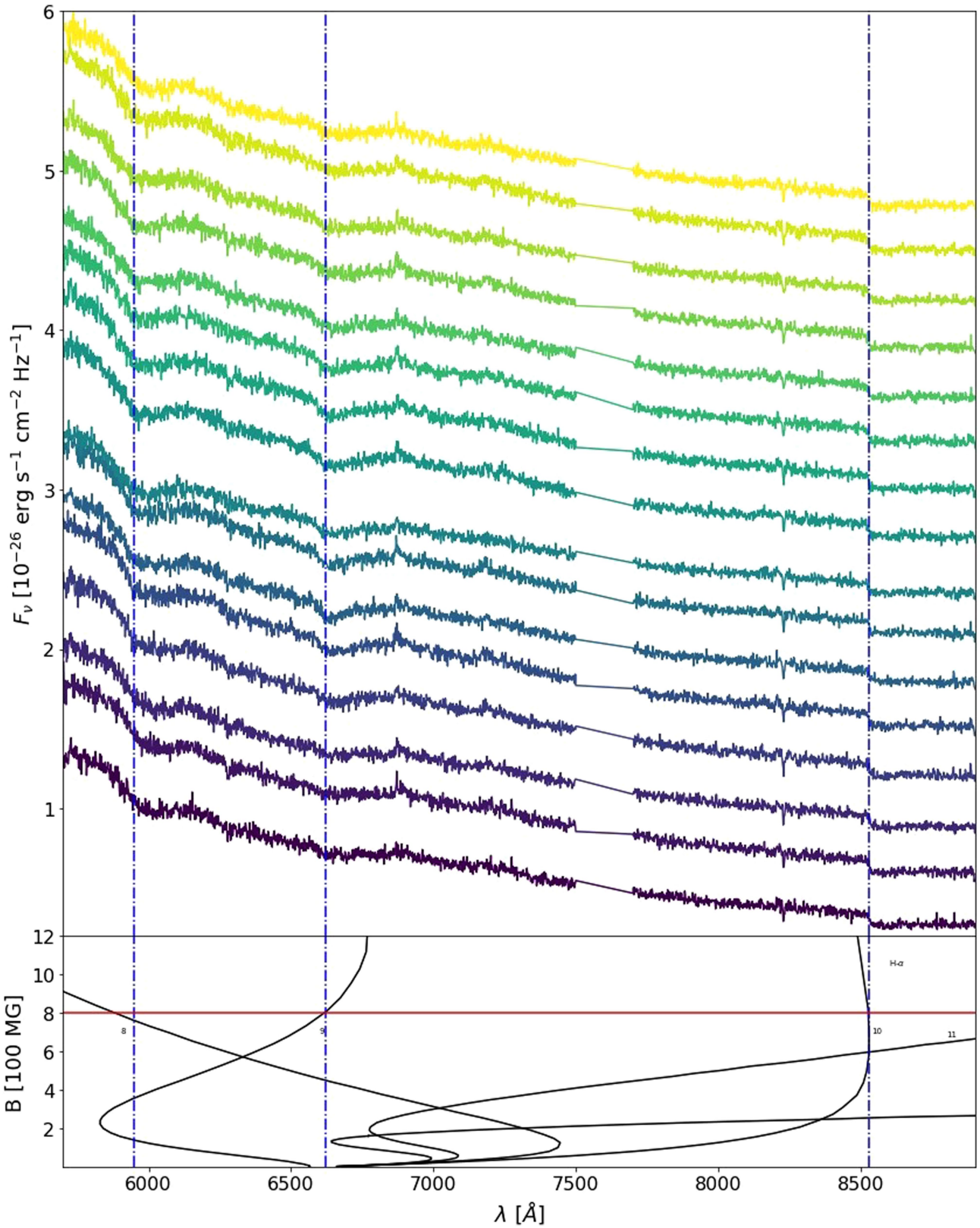

Extended Data Fig. 5 | Phase-resolved spectra, red side. The LRIS phase-resolved spectra of ZTF J1901+1458 in the red side. Some small variations can be observed in the spectral features with phase: in particular, the feature at ~6,620 Å becomes broader and narrower with phase.

Extended Data Table 1 | Photometric data for ZTF J1901+1458

PS1$-z$	PS1$-i$	PS1$-r$	PS1$-g$
16.595 ± 0.006	16.276 ± 0.003	15.977 ± 0.003	15.513 ± 0.002
UVOT$-U$	UVOT$-UVW1$	UVOT$-UVM2$	UVOT$-UVW2$
14.94 ± 0.06	14.42 ± 0.06	14.40 ± 0.06	14.38 ± 0.06

Extended Data Table 2 | Identified Balmer transitions

	line	$nlm \rightarrow n'l'm'$	$NM\mu \rightarrow N'M'\mu'$	λ [Å]
1	Balmer Hγ	$2s_0 \rightarrow 5p'_0$	0 0 2 $\rightarrow$ 0 0 11	3344.23
2	Balmer Hγ	$2s_0 \rightarrow 5p'_{-1}$	0 0 2 $\rightarrow$ 0 $-$1 10	3370.41
3	Balmer Hγ	$2s_0 \rightarrow 5f'_0$	0 0 2 $\rightarrow$ 0 0 9	3464.11
4	Balmer Hβ	$2s_0 \rightarrow 4p'_0$	0 0 2 $\rightarrow$ 0 0 7	3694.56
5	Balmer Hβ	$2s_0 \rightarrow 4p'_{-1}$	0 0 2 $\rightarrow$ 0 $-$1 6	3805.82
6	Balmer Hβ	$2s_0 \rightarrow 4f'_0$	0 0 2 $\rightarrow$ 0 0 5	4249.86
7	Balmer Hβ	$2s_0 \rightarrow 4f'_{-1}$	0 0 2 $\rightarrow$ 0 $-$1 4	4517.97, 4590.9
8	Balmer Hα	$2p_{-1} \rightarrow 3d_{-2}$	0 $-$1 0 $\rightarrow$ 0 $-$2 0	5883.63
9	Balmer Hα	$2s_0 \rightarrow 3p_0$	0 0 2 $\rightarrow$ 0 0 3	6615.06
10	Balmer Hα	$2p_0 \rightarrow 3d_{-1}$	0 0 2 $\rightarrow$ 0 $-$1 1	8525.69
11	Balmer Hα	$2s_0 \rightarrow 3p_{-1}$	0 0 1 $\rightarrow$ 0 $-$1 2	8537.76, 9542.62

The numbers correspond to the identified transitions in Fig. 3, and the wavelengths of the transitions at 800 MG are from ref. [13]. For 7 and 11, we also list the wavelength for 600 MG (left).